communications physics

A Nature Portfolio journal

Article

https://doi.org/10.1038/s42005-025-02155-5

Dissipative solitons signature in achiral Néel magnetic domain walls driven by spin-orbit torque

Check for updates

Mouad Fattouhi [1] ✉, **André Thiaville** [2], **Felipe García-Sánchez** [1,3], **Ruben M. Otxoa** [4,5], **María Pilar García Estévez** [6], **Eduardo Martínez** [1,3] & **Luis López-Díaz** [1,3]

Magnetic domain walls offer a compelling platform for investigating non-linear spatio-temporal phenomena due to their rich internal dynamics under external stimuli. Here, we investigate the dynamics of achiral Néel domain walls (DWs) driven by spin-orbit torque in wide ferromagnetic strips. Our study reveals that these DWs cease motion above a certain threshold current density, while their internal magnetic moments exhibit a spatial modulation characterized by a 180° rotation leading to a quasi-sinusoidal distortion of their shape. Unlike achiral DWs in narrow strips, which stop because they take on a Bloch configuration, achiral DWs in wide strips stop due to the internal diffusive torques originating from exchange interaction that counterbalance locally the torques contributing to the DW dynamics. If these torques are perfectly balanced, the DW remains stationary, whereas the slighter imbalance triggers complex nonlinear dynamics, including continuous oscillation of the domain wall magnetization or quasi-periodic explosions in which the domain wall "cracks" and recovers its structure afterwards. Our findings unveil a dissipative solitonic signature in achiral domain walls driven by SOT, akin to dissipative solitons observed in other scientific fields. This work paves the way for exploring nonlinear spatio-temporal dynamics in DWs with potential applications in logic and neuromorphic computing.

Due to the interplay of nonlinear dynamics, dissipative processes, and external perturbations, complexity and order can coexist in non-equilibrium systems, which often leads to the emergence of intricate patterns[1–3]. The pioneering work of Alan Turing on reaction–diffusion equations revealed how simple local interactions can lead to complex spatial patterns from homogeneous uniform states[4]. Since then, tremendous efforts have been devoted to understanding the origin of patterns and their stability in various disciplines, including Chemistry, Biology, and Physics[5,6]. In Physics, pattern formation manifests itself in different systems, including Rayleigh–Benard convection[7], Taylor-Couette flow[8], laser fibers[9], and magnetic films[10].

Understanding concepts like pattern formation and self-organization was essential to develop the notion of dissipative solitons[3]. Dissipative solitons are localized structures that exist for an extended time period in open systems far from equilibrium under energy supply[11]. In contrast to classical solitons, which originate only from the balance between dispersion/diffusion and nonlinear effects, dissipative solitons also fulfill a balance between the gain and loss of energy, since they usually appear far from equilibrium. Therefore, these solitons are not subject to energy, speed, or shape conservation laws[12]. Dissipative solitons have been observed in different areas, such as fluids, photonics, and magnetism[13]. Some examples include spirals[14], rogue waves[15], and magnetic droplet solitons[16].

Pattern formation is ubiquitous in magnetic ordered media, where magnetic textures such as skyrmions, vortices, or domain walls (DWs) are being extensively investigated these days because, among other things, they are considered potential candidates for neuromorphic computing technologies due to their complex nonlinear behavior[17]. Among magnetic textures, domain walls stand out as a particularly fertile platform for exploring nonlinear phenomena[18,19]. When subject to external stimuli such as a magnetic field or spin transfer torque (STT), DWs exhibit two different regimes. First, the steady regime, wherein the DW, after a brief transient period, reaches a steady state where its velocity scales linearly with the

[1]Departamento de Fisica Aplicada, Universidad de Salamanca, Salamanca, Spain. [2]Laboratoire de Physique des Solides, Université Paris-Saclay, CNRS, Orsay, France. [3]Unidad de Excelencia en Luz y Materia Estructuradas (LUMES), Universidad de Salamanca, Salamanca, Spain. [4]Hitachi Cambridge Laboratory, CB3 OHE Cambridge, Cambridge, UK. [5]Donostia International Physics Center, San Sebastian, Spain. [6]Departamento de Fisica Fundamental, Universidad de Salamanca, Salamanca, Spain. ✉e-mail: mfa@usal.es

external force strength. Second, if the external force exceeds a certain threshold strength, the DW exhibits the so-called Walker breakdown, where it transitions into an oscillatory regime characterized by intricate nonlinear changes in both its velocity and internal magnetization[20]. It has been shown that during the oscillatory regime, the internal magnetization of DWs in narrow strips depicts a uniform precessional behavior with negligible spatial variations[21]. On the other hand, DWs in wider strips were shown to exhibit more complex spatio-temporal dynamics, wherein patterns such as vertical Bloch lines (VBLs) eventually appear[22]. Previous investigations have shown that the motion and interaction of VBLs result in a pure precessional dynamics of the DW, since a perpetual process takes place in which VBLs are continuously nucleated in pairs inside the DW and annihilated at the edges, resulting in a decrease in the speed of the translational movement of the wall[23,24]. However, in the case of Néel DWs stabilized via interface Dzyaloshinskii–Moriya interaction (iDMI), VBLs were shown to move at different velocities due to the broken symmetry. This velocity mismatch leads to the annihilation of neighboring VBLs by collision and results in a saturation of the DW velocity around a certain value that depends on the iDMI field[25].

Here, we investigate the dynamics of Néel DWs driven by spin-orbit torque (SOT) and stabilized via in-plane uniform strain. We demonstrate that, due to their achiral nature and the interplay between the different torques involved, these DWs display unique behavior and depict several nonlinear states, including complex spatio-temporal patterns. This is due to the extreme sensitivity of the SOT to the domain wall magnetization, in stark contrast to field-driven or STT-driven DW motion. We show that these achiral DWs move with a quasi-linearly increasing velocity as the current density increases. When reaching a threshold current density, they cease movement entirely and remain immobile regardless of further increases in current density. Simultaneously, the DW internal magnetization depicts a spatial pattern characterized by a swirling of the DW magnetic moments and distortions of its shape. Using micromagnetic simulations (μM) and analytical models, we characterize the formed pattern as a 180°-kink with ripple-like distortions of the DW shape, and we identify the key factors contributing to the formation of these kinks during the transient dynamics. Subsequently, we demonstrate that above the threshold, the system suffers multiple bifurcations, leading to an increase in the number of kinks inside the DW as the current increases. We find that the passage from a state with a number of kinks k to a state with $k+1$ can be accompanied by a critical transition where the DW exhibits spatio-temporal patterns with intricate nonlinear behavior. In particular, we observe two distinct situations. First, there is a pulsating DW behavior, where the DW changes its structure and shape continuously over time. Second, an exploding DW behavior occurs, where the DW passes a quasi-static phase, then cracks (i.e., becomes multiple) and recovers its structure periodically. We discuss these two regimes with respect to dissipative solitons found in other physical systems described by the complex Ginzburg–Landau, reaction–diffusion, and Swift–Hohenberg equations[11,26]. This work explores complex spatio-temporal nonlinear DW dynamics and reports the first theoretical prediction of DWs solitonic pulsation and explosion.

Results and discussion

SOT-driven dynamics of achiral Néel DWs

The system under study is schematically represented in Fig. 1a. It consists of a long nanostrip of width W and thickness t_{FM} made of a ferromagnet with strong perpendicular magnetic anisotropy and a Néel DW located at the center. The nanostrip is subject to a longitudinal uniform strain ε_{xx} strong enough to favor the Néel configuration over the Bloch one. It was recently shown[27] that by inducing a sufficiently strong in-plane anisotropy, it is possible to stabilize achiral Néel DWs in the absence of interfacial DMI, and in[28] we showed that this can be achieved using longitudinal strain ε_{xx}. As indicated in Fig. 1a, our DW is also subject to an SOT induced by a charge current J flowing through an adjacent heavy metal underneath, which pushes the DW along the $+x$ direction.

Figure 1b shows the DW average velocity versus applied current obtained from μM simulations of different widths, together with the prediction of a one-dimensional (1D) model in terms of the DW position q and its internal angle ψ (see Supplementary Note 1 for details). As can be

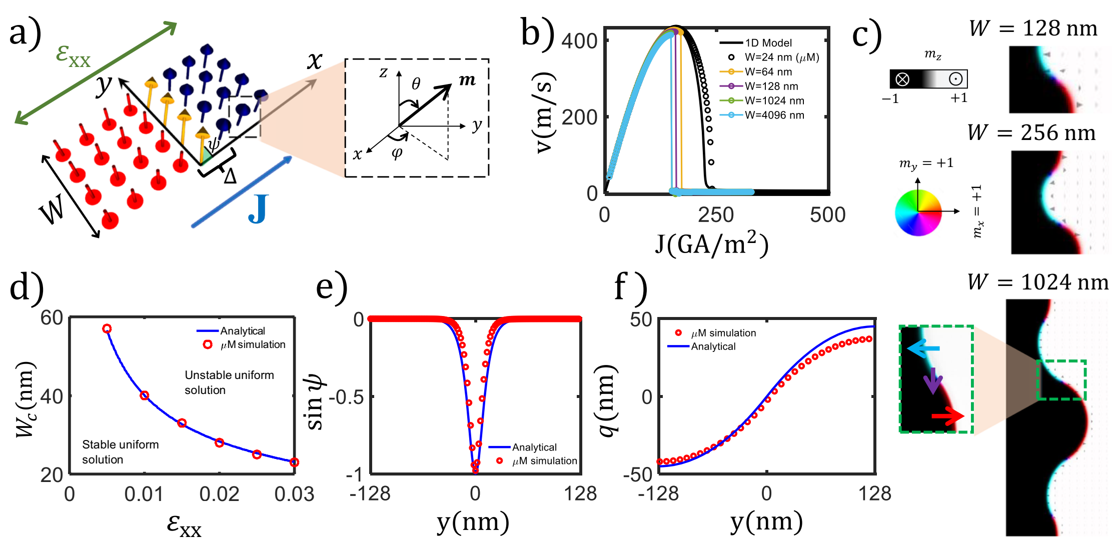

Fig. 1 | Achiral Néel domain wall (DW) under spin-orbit torque (SOT). **a** Schematic representation of the studied device; a Néel DW located in the center of a magnetic film and subject to an in-plane longitudinal strain ε_{xx} and SOT induced by a charge current J. Note that ψ is the DW angle and φ denotes the azimuthal angle of the magnetization in spherical coordinates. **b** DW average velocity versus applied current density for different strip widths (W) computed from micromagnetic (μM) simulations for a 50 ns time window and compared to the 1D Model predictions. **c** Micromagnetic snapshots of the DW structure for J = 175 GA/m^2 and different widths W for a 100 ns time window. The inset shows a magnification of the magnetic moments modulations inside the DW. **d** Critical width for unstable uniform solution of the system (i.e., unstable 1D behavior) versus the in-plane strain from both micromagnetic simulation and a linear stability analysis of Eq. (1) and Eq. (2). **e** Magnetization component $m_y = \sin\psi(y)$, plotted along y-axis from both Eq. (3) and simulation for W = 256 nm, J = 200 GA m^{-2} and ε_{xx} = 0.02. **f** DW displacement q, plotted along the $y-$ axis from both Eq. (4) and simulation for W = 256 nm, J = 200 GA m^{-2}, and ε_{xx} = 0.02.

observed, this 1D model predicts that the DW velocity initially increases with current up to approximately 160 GA m^{-2} and then starts decreasing gradually until it becomes null at roughly 240 GA m^{-2}, remaining zero for larger current values. As explained in ref. 29, this behavior is due to the fact that, by increasing the current, the DW internal angle gradually tilts from a Néel $\left(\psi = 0, \pi\right)$ to a Bloch configuration $\left(\psi = \pm\frac{\pi}{2}\right)$, which reduces the SOT efficiency[30]. A similar behavior is obtained from μM simulations for the narrowest nanostrip ($W = 24$ nm), which indicates that the DW behaves like a rigid 1D object (i.e., with uniform magnetization along the transverse direction y-axis) in this case. For the other cases, however, the initial regime of linearly increasing velocity remains practically unchanged, but, instead of getting a gradual decreasing regime, the DW abruptly comes to a complete stop when a certain critical current J_c is reached, which is a clear indication that the DW deviates from the 1D behavior. This becomes evident if one looks at Fig. 1c, where we show typical snapshots of the magnetization for three different strip widths and an applied current above the critical one. These snapshots correspond to the steady state, once the DW has stopped motion, and as can be observed, in the three cases, the DW presents a regular undulating structure consisting of a concatenation of segments of the same curvature strength but with alternating sign. In the enlarged area (see the inset in Fig. 1c), we present a detailed view of the transition region separating two consecutive segments magnetized along positive $+x$ (right) and $-x$ (left) directions, respectively. In the transition region, which extends only over a few nanometers, the magnetization points along $-y$ direction. Despite the fact that these structures belong to the Bloch lines (BLs) family, we will refer to them as *kinks* in what follows for the sake of simplicity.

Considering the two-dimensional structures shown by the DWs (Fig. 1c) and with the aim of getting a good understanding of their features and the dynamic processes that lead to them, we generalized the 1D model mentioned above, allowing both DW coordinates q and ψ to vary along the transversal coordinate of the nanostrip y. This generalization results in two partial differential equations describing the DW dynamics known as Slonczewski equations[31] (see Supplementary Note 2 for detailed derivation)

$$(1+\alpha^2)\frac{\partial_t q}{\Delta} = \alpha\mathcal{D}\frac{\partial_{yy} q}{\Delta} - \alpha\Gamma_{\rm SOT} - \mathcal{D}\partial_{yy}\psi + \Gamma_{\rm AN} \tag{1}$$

$$(1+\alpha^2)\partial_t \psi = \mathcal{D}\frac{\partial_{yy} q}{\Delta} - \Gamma_{\rm SOT} + \alpha\mathcal{D}\partial_{yy}\psi - \alpha\Gamma_{\rm AN} \tag{2}$$

where $\mathcal{D} = \frac{2\gamma_0 A_{ex}}{\mu_0 M_s}$ is a diffusive-like constant in m^2/s unit, $\Gamma_{\rm SOT} = \frac{\gamma_0\pi}{2}H_{\rm SOT}\cos\psi$ is the SOT with $H_{\rm SOT} = \frac{\hbar\theta_{sh}J}{2|e|\mu_0 M_s t_{\rm FM}}$ the SOT field. $\Gamma_{\rm AN} = \gamma_0 H_{\rm AN}\sin 2\psi$ is the in-plane anisotropy torque, with $H_{\rm AN} = \frac{H_{\rm sh}}{2} - H_{\rm mel}\varepsilon_{\rm xx}$ being the in-plane anisotropy field including both the magnetoelastic and shape contributions, and $\Delta = \sqrt{\frac{A_{ex}}{K_{\rm eff}}}$ is the DW width as sketched in Fig. 1a with $K_{\rm eff} = K_u - \frac{1}{2}\mu_0 M_s^2$. The shape and magnetoelastic anisotropy fields are defined as $H_{\rm sh} = M_s\left(N_y - N_x\right)$ and $H_{\rm mel} = \frac{B_1}{\mu_0 M_s}$ respectively.

Physically, Eq. (2) describes the dynamics of the in-plane DW magnetization angle as a precession driven by the SOT, augmented by a cross-diffusive term ($\partial_{yy}q$) related to the DW curvature, reflecting the familiar surface tension effect[32]. The damping moderates this precession according to the anisotropy field and by a diffusive term smearing out the angle inhomogeneities ($\alpha\partial_{yy}\psi$). Similarly, Eq. (1) expresses the dynamics of the DW position q as a function of the anisotropy field and a cross-diffusive term ($\partial_{yy}\psi$) related to spatial modulation of the DW magnetization. Damping affects q according to the SOT, and also via the diffusion term ($\alpha\partial_{yy}q$), which smooths out its spatial inhomogeneities.

A linear stability analysis of Eq. (1) and (2) (refer to supplementary note 3 for more details) suggests that around a certain strip width $W_c = \pi\sqrt{\frac{A_{ex}}{K_{\rm sh} - B_1\varepsilon_{\rm xx}}}$ the uniform solution is no longer stable and the internal DW structure should exhibit a non-uniform pattern, as in fact can be seen in Fig. 1c. In Fig. 1d, we illustrate this critical width versus in-plane strain, computed from the analytical model, and compared to simulations. Both approaches agree on predicting the phase boundary, differentiating the pure 1D domain wall behavior from the intricate 2D behavior observed for wider strips in Fig. 1b, c.

In order to gain a deeper understanding of the DW internal structure, we solve Eq. (1) and (2) analytically in the steady state (i.e., $\partial_t q = \partial_t\psi = 0$) to get both the space dependent DW angle $\psi(y)$ as well as the corresponding DW displacement $q(y)$ (see Supplementary Note 2 for further details about the used boundary conditions)

$$\psi(y) = 2\tan^{-1}\left[e^{\frac{-Qy}{\lambda}}\right] \tag{3}$$

$$q(y) = \frac{\Omega}{2}\left[y^2 + Wy + \lambda^2\left(\mathrm{Li}_2(-e^{\frac{2y}{\lambda}}) + \frac{\pi^2}{12}\right)\right] \tag{4}$$

where $\lambda = \sqrt{\frac{A_{ex}}{K_{\rm sh} - B_1\varepsilon_{\rm xx}}}$ is the kink transition width with $K_{\rm sh} = \frac{1}{2}\mu_0 M_s^2(N_y - N_x)$, $Q = \pm 1$ denotes the orientation of the magnetization around the kink transition, $\Omega = -Q\frac{\pi\Delta\hbar\theta_{\rm SH}J}{8eA_{ex}t_{\rm FM}}$ and $\mathrm{Li}_2(x)$ is the Spence function[33].

Figure 1e, f shows the profile of $\sin\psi(y)$ and $q(y)$ along y for $W = 256$ nm computed from both simulations and Eqs. (3) and (4) respectively. As can be observed in both figures, the DW internal structure in the steady state is well predicted by the model. The internal twist of the DW takes the form of a 180°-kink where the DW angle at the kink transition is always pointing towards the $-y$ direction (i.e., $\psi(y) = -\frac{\pi}{2}$) as one can confirm also from Fig. 1c. This orientation is a direct consequence of the spin current polarization ($\boldsymbol{H}_{\rm SOT}||\boldsymbol{\sigma}$), which breaks the symmetry and allows for only one possible orientation at the kink. This phenomenon results in a 2-fold degeneracy within the system, leading to only two possible kink structures: either transitioning from a $+x$ orientation to a $-x$ one with $Q = +1$ or vice versa with $Q = -1$. This behavior can also be understood from the linear stability analysis, which, as mentioned before, indicated that at the critical width the uniform solution becomes unstable and a stationary bifurcation takes place. Instead, two distinct non-uniform solutions emerge, each characterized by a different value of Q. When examining the displacement $q(y)$, we observe that the DW shifts in opposite directions around the kink transition. This behavior is due to the $\cos\psi(y)$ dependence of $\Gamma_{\rm SOT}$, so that the force pushing the DW is of opposite sign on each side of the kink, which forces the DW to adopt a ripple-like shape to achieve stability (see Fig. 1c). We can infer from Eq. (4) that the amount of DW stretching is a compromise between the SOT and exchange, which becomes evident as $\Omega \propto \frac{J}{A_{ex}}$. This anticipates the crucial role that the DW elasticity is poised to play in its structure as well as its stability, as we explore in the following.

Transient dynamics and kinks stabilization

Up to this point, we have observed that achiral DWs driven by SOT stop moving above a certain threshold current, and their internal magnetization exhibits 180° kinks in equilibrium. Now, let us focus on understanding the transient regime, including the mechanisms leading to DW stabilization and the kinks formation.

Kink nucleation is initially triggered by the precessional component of the SOT ($\Gamma_{\rm SOT}$), which, when the current is above the threshold, forces the internal magnetic moments of the DW to tilt from their equilibrium values ($\psi(y) = 0, \pi$). This is shown in Fig. 2 where we plot all the torques involved in Eq. (2) as a function of y at different times. Due to the inhomogeneity of the demagnetizing field near the DW boundaries[34,35], its internal magnetic moments there rotate with different angular velocity with respect to those located far from the strip edge, as shown in Fig. 2b. As soon as neighboring moments in arbitrary regions along the DW start exhibiting large non-colinearities (see the yellow circles in Fig. 2b) the exchange energy increases,

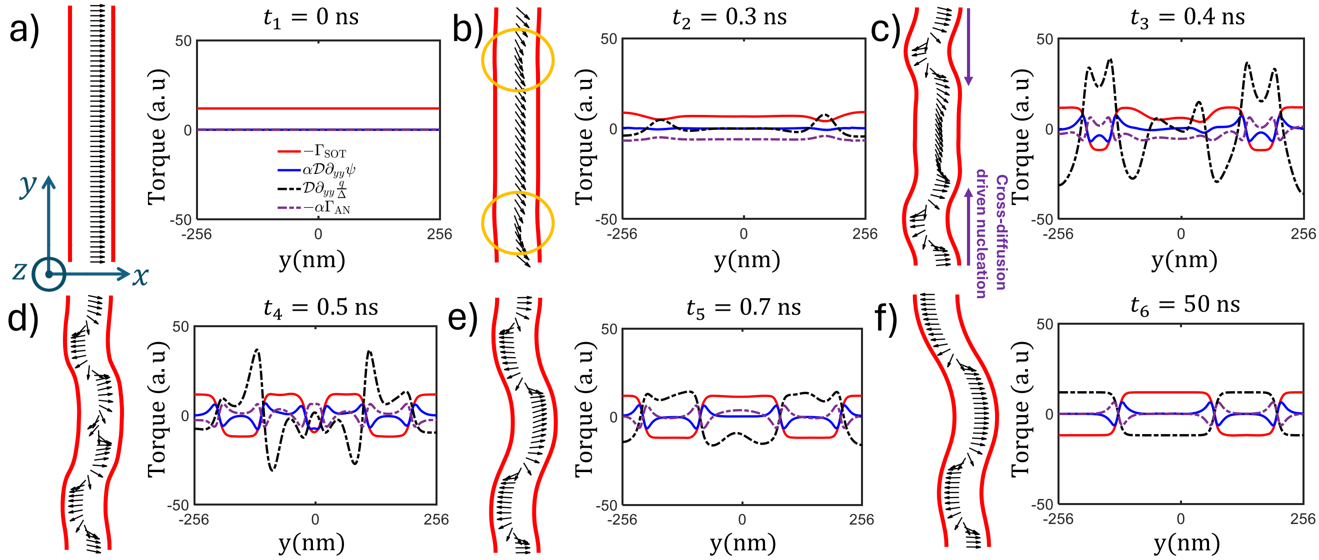

Fig. 2 | Kinks nucleation in the transient regime. Arrow representation of the domain wall (DW) internal magnetic moments as well as the spatial profile of the torques involved in Eq. (2) for a width $W = 512$ nm and a current value well above the critical one $J = 170$ GA m$^{-2} > J_c$. **a** $t = 0$ ns. **b** $t = 0.3$ ns, the yellow circles indicate the non-coherent rotation of moments near the boundaries compared to those at the center. **c** $t = 0.4$ ns, the purple arrows indicate the cross-diffusion driven nucleation. **d** $t = 0.5$ ns. **e** $t = 0.7$ ns. **f** $t = 50$ ns.

thus the ones with the largest tilting reverse due to the cross-diffusive torque ($\mathcal{D}\partial_{yy}q$). This leads to the nucleation of kink pairs, which insures a gradual transition of the magnetic moments inside the DW and therefore reduces the exchange energy cost (see black arrows in Fig. 2c). When the first kink pairs appear, the nucleation continues spreading along the DW due to the cross-diffusive torque, as can be noticed from Fig. 2d. This becomes evident if we check the dominant torque after the first nucleation event (at t_3) as shown in Fig. 2c. In fact, it is well known that diffusion itself does not promote pattern formation in physical systems, but instead it tries to smooth spatial irregularities. However, in our particular situation, kink nucleation is driven by the off-diagonal terms of the diffusion matrix (i.e., cross-diffusive terms) ($\mathcal{D}\partial_{yy}q$ and $-\mathcal{D}\partial_{yy}\psi$), which appear due to magnetization precession. This pattern formation is, therefore, similar to other cross-diffusion patterns formed in reaction–diffusion systems, such as Turing spots and strips[36–38].

Right after the nucleation regime, the kinks enter a quasi-static regime during which they evolve slowly before eventually reaching a steady state. The post-nucleation regime was found to be much slower compared to the nucleation one (characteristic time for nucleation is t_n~0.1 ns, whereas for stabilization it is around t_f~10–100 ns in most cases). During the slow evolution regime, some of the kinks annihilate by colliding with each others or hitting the strip edges, as can be clearly observed from the Supplementary Movies 1 and 2, where we show the process depicted in Fig. 2 from both simulation and the numerical solution of Eq. (1) and (2). Afterward, the DW reaches a steady state where the diffusive torques compensate the other two torques involved in its dynamics, as confirmed in Fig. 2f. As can be remarked from the supplementary movie 1, our model provides a good prediction of the DW transient dynamics and captures all the essential events, including kinks annihilation by kink–kink or kink–edge collisions as well as the ripple-like shape of the DW displacement. It is important to note that, due to topological selection rules, kink nucleation always occurs in pairs with opposite winding numbers[39]. However, the total topological charge of the system is not conserved, as some kinks are annihilated through kink–edge interactions caused by finite-size effects.

In Fig. 3a, we show the time evolution of m_y along the transversal coordinate y for three cases with different widths (W) from both simulations and the numerical solution of Eq. (1) and (2). As can be observed in this figure, after kink nucleation, the system evolves in time, and some kinks are annihilated by colliding with each other or with the boundary of the system. This mechanism leads to a total compensation of the torques involved in Eq. (1) and (2) and, eventually, the DW reaching equilibrium. At this point, we can reveal the difference between the physical mechanisms upon which the DW stops in narrow and wide strip cases. While 1D DWs confined in narrow strips stop motion due to the torques vanishing (see Supplementary Note 1 for further explanation)[29], DWs in wider strips, as shown in our study, stop moving due to the emergence of diffusive torques from exchange interaction, which balance the other torques contributing to the dynamics. As will be shown in the following, this will lead to a rich dynamic scenario with different states that cannot take place in 1D DWs.

In Fig. 3b, we plot the evolution of the number of kinks k versus the applied current density J for different strip widths W. For a fixed value of J, the number of kinks increases as the strip becomes wider. This increase can be intuitively understood by considering the system characteristic length scales $\ell_\psi = 2\pi\sqrt{\frac{\mathcal{D}}{2\omega_{AN}}}$ and $\ell_q = 2\pi\sqrt{\frac{2\alpha\mathcal{D}}{2\alpha\omega_{AN}-\omega_{SOT}}}$, which are on the order of tens of nanometers as estimated from the dispersion relation analysis (see Supplementary Note 4 for further details). $\omega_{SOT} = \gamma_0\frac{\pi}{2}H_{SOT}$ and $\omega_{AN} = \gamma_0 H_{AN}$ are the SOT and in-plane anisotropy pulsations, respectively. As W increases, a higher degree of spatial modulation is possible, leading to a higher number of kinks. Similarly, increasing J for a fixed W induces an increase in k. This effect cannot be explained simply by using the length scale argument. This is because the current is not only affecting ℓ_q but also influences the DW stretching amplitude as anticipated in the previous subsection, where in the steady state this amplitude was found to be proportional to $\Omega \propto J/A_{ex}$.

To get a better understanding of the mechanisms that trigger this increase in k with the applied current, we decided to examine how the DW length ℓ_{DW} and its energy evolve as J increases. To do so, we focus on the case with $W = 256$ nm and compute the DW length from micromagnetic simulations using (see Supplementary Note 5 for further details)

$$\ell_{DW} = \int_0^W \sqrt{1 + \left(\frac{\mathrm{d}q(y)}{\mathrm{d}y}\right)^2}\,\mathrm{d}y \tag{5}$$

On the other hand, we use a simple model to calculate the full DW energy as the sum of the kinks energies and the background Néel DW over

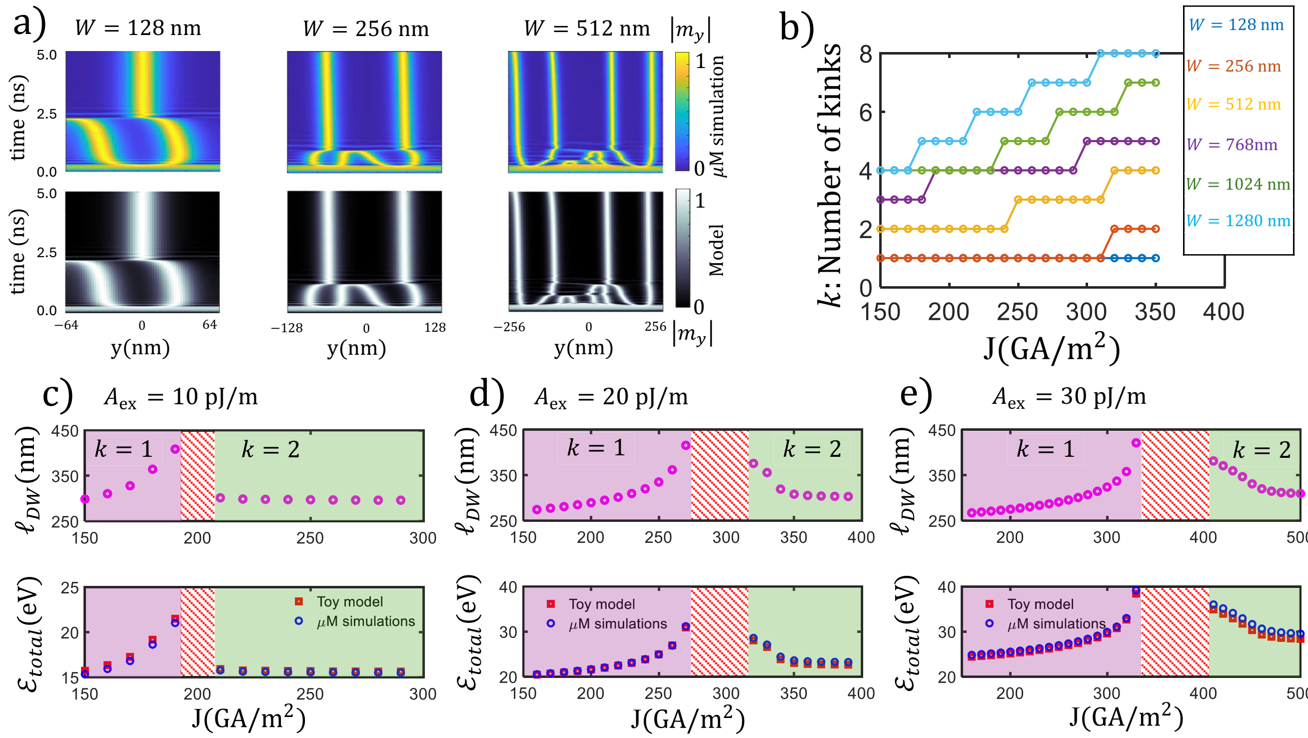

Fig. 3 | Kinks bifurcation. **a** Spatio-temporal diagrams of the transverse magnetization component $|m_y|$, from both simulations and the numerical solution of the model (Eq. (1) and (2)) for an applied current $J = 225$ GA m^{-2} and the different strip widths $W = 128$ nm, $W = 256$ nm, and $W = 512$ nm. **b** Number of kinks k at the steady or quasi-steady states versus applied current for strips with different widths computed via simulations. Domain wall (DW) length (ℓ_{DW}) computed from simulation and total energy $\mathcal{E}_{\text{total}}$ from both simulations and the toy model in Eq. (6) versus current for a strip width $W = 256$ nm and different exchange stiffness constants A_{ex}: **c** $A_{ex} = 10$ pJ m^{-1}, **d** $A_{ex} = 20$ pJ m^{-1}, **e** $A_{ex} = 30$ pJ m^{-1}.

which the kinks are stabilized

$$\mathcal{E}_{\text{total}} = N\mathcal{E}_{kink} + \mathcal{E}_{DW} \tag{6}$$

where N is the total number of kinks, $\mathcal{E}_{kink} = 4N\Delta t_{FM}[\frac{A_{ex}}{\lambda} + \lambda(K_{sh} - B_1\varepsilon_{xx})]$ is the kink energy, and $\mathcal{E}_{DW} = 2t_{FM}[\frac{A_{ex}}{\Delta}(\ell_{DW} - \lambda N) + \Delta(K_{eff} + B_1\varepsilon_{xx})(\ell_{DW} - \lambda N)]$ is the energy of a Néel DW. Although this simple model does not directly account for the DW curvature, such an effect is implicitly included via the DW length ℓ_{DW}.

In Fig. 3c–e, we show both the DW length and its total energy versus J for $W = 256$ nm and three different values of the exchange stiffness constant A_{ex} after 1 µs. Simulation results for the DW energy are also compared to the ones obtained from Eq. (6) in the bottom graphs. It can be perceived from Fig. 3c–e how both DW length and energy increase with J. Around a certain critical current density, both ℓ_{DW} and $\mathcal{E}_{\text{total}}$ increase markedly, leading to a transition towards an unstable regime and then to a state with $k = 2$. The appearance of a second kink minimizes the DW energy and recovers the system stability as can be noticed from Fig. 3c–e (the green shaded parts). The DW deformation $\varepsilon_{\text{DW}} = (\ell_{DW} - W)/W$ at the critical transition was found around ε_{DW}~0.6 for the three values of A_{ex}, and we can observe that the higher the exchange stiffness, the higher the current density needed to reach the critical transition. The mechanism observed here can be explained as follows. After the nucleation phase, the number of kinks is initially determined by the system characteristic length scales ℓ_ψ and ℓ_q, as explained previously in this section. Once the number of kinks stabilizes according to these length scales, the applied current stretches the DW until it reaches a stable state with the torques balanced, as explained before. When the applied current increases to the point where it pushes the DW to its stretching limit, a transition occurs towards a non-stationary state, as indicated by the red dashed regions in Fig. 3c–e. Further increasing the current reduces ℓ_q, allowing the stabilization of a new kink, which reduces the DW length and its energy, allowing it to recover a stationary state where all torques are balanced again. It is worth noting that the transition from k to $k + 1$ is usually accompanied by a critical regime where the DW exhibits non-stationary behavior and undergoes more intricate nonlinear dynamics.

Non-stationary regimes and dissipative solitons signature

In Fig. 4 we present the spatio-temporal plot of the transverse magnetization component $|m_y|$ as well as the temporal evolution of its spatial average $\langle m_y \rangle$ for $W = 256$ nm and three different current densities. In Fig. 4a, which corresponds to $J = 170$ GA m^{-2}, we observe that, after kink nucleation, the DW slowly evolves towards a steady state where a single kink is stabilized. In this situation, the system reaches a stationary state because the diffusive torques are able to balance the SOT and the anisotropy torque. During this stationary regime, the DW remains static, and its internal structure does not undergo any changes as long as the applied current is sustained (see Supplementary Movie 3). Increasing the applied current density to $J = 280$ GA m^{-2} leads the internal DW magnetization to oscillate continuously (see Fig. 4b). In this case, the DW recovers its translational dynamics, moving along the strip while continuously altering its shape (see Supplementary Movies 4 and 6). From the plot of the average magnetization $\langle m_y \rangle$ in Fig. 4b, we can see that these oscillations take a packet-like form with a frequency f~0.4 GHz (see zoomed area in Fig. 4b). If the current density is increased further, the DW exhibits even more intricate spatio-temporal dynamics as displayed in Fig. 4c. In this situation ($J = 460$ GA m^{-2}), we observe a striking behavior. Namely, the DW, after the kinks nucleation phase, enters a quasi-static regime and then, suddenly, cracks to multiple domains (the red dashed box in Fig. 4c) but recovers its structure and re-exhibits this process continuously over time (green dashed box in Fig. 4c).

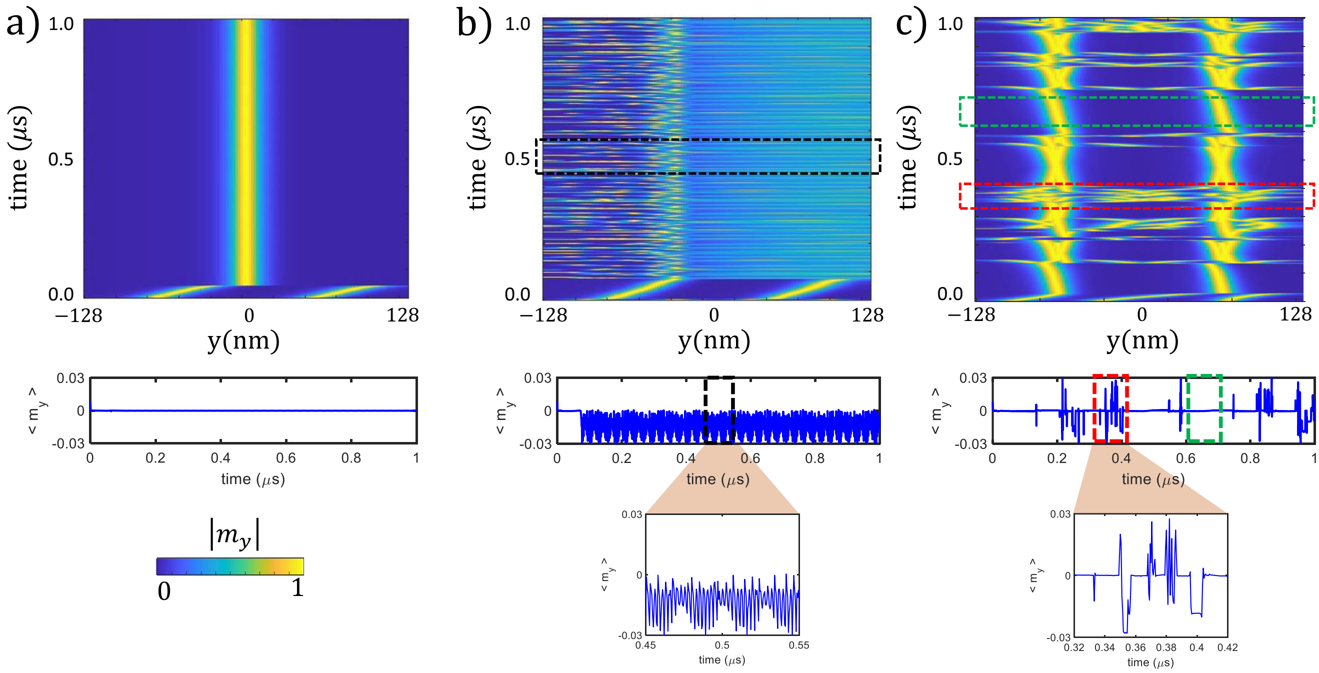

Fig. 4 | Domain wall dissipative solitonic behavior. Spatio-temporal plots of the transverse magnetization component $|m_y|$ and the temporal evolution of its spatial average $\langle m_y \rangle$ for a strip with $W = 256$ nm from simulations (dashed boxes indicate the zoomed areas in the bottom panels). The color bar represents transverse magnetization component $|m_y|$. **a** Current density $J = 170$ GA m^{-2}. **b** Current density $J = 280$ GA m^{-2}. **c** Current density $J = 460$ GA m^{-2}. This figure is better understood if seen with the Supplementary Movies 3, 4, and 5, respectively.

The average magnetization in this case depicts a spiking behavior, as can be observed from the plot of the average magnetization $\langle m_y \rangle$ in Fig. 4c. Such an explosive process is shown in the supplementary movie 5.

The results in Fig. 4 reveal a signature of dissipative solitons in the dynamics of achiral DWs driven by SOT. First, the behavior in Fig. 4a is similar to stationary dissipative solitons that occur in dissipative nonlinear systems when the balance between dispersive/diffusive and nonlinear effects on one hand, and energy gain and loss on the other, is fulfilled[11]. This kind of soliton exists as long as the energy supply is maintained, and they vanish otherwise. Second, the behavior shown in Fig. 4b is analogous to a pulsating dissipative soliton that takes place when the balance of dispersion/diffusion and non-linearity is slightly perturbed[40]. This kind of soliton is known to exhibit different oscillatory phenomena depending on the type of bifurcation in the system. Furthermore, they provide a good platform for chaotic phenomena[41]. Finally, the situation in Fig. 4c is a typical signature of exploding dissipative solitons that emerges when non-linearity dominates over the dispersion/diffusion or when the energy gain is relatively important to dissipation[42,43]. This exploding soliton scenario provides a route to investigate chaotic phenomena in magnetic systems[40]. The dissipative solitons' signature occurs in the achiral DWs due to the fact that their dynamics is governed by the interplay between diffusive and nonlinear torques.

We believe that the dynamic states exhibited by achiral Néel DWs driven by SOT that we have just shown theoretically can be verified experimentally using thin film device fabrication technology and state-of-the-art imaging techniques such as Kerr microscopy[44]. To drive the proposed achiral Néel DWs with SOT, the fabricated device should exhibit a negligible interfacial DMI while maintaining a significant Spin Hall effect (SHE), which underlies the generation of SOT. To achieve such devices, tri-layer structures with a ferromagnet sandwiched between two heavy metal layers of the same material but with different thicknesses can provide a zero net DMI due to symmetric interfaces[45]. However, these structures can still exhibit a non-vanishing SHE due to the different current densities flowing through the two heavy metal layers. Along the same lines, it has been demonstrated that inserting a metallic spacer at the interface of heavy metals and ferromagnets can suppress interfacial DMI while enabling spin current injection, which contributes to SOT[46,47]. Beyond the device architecture, other factors must be considered in the experimental context, such as structural disorder and thermal effects.

The behavior of achiral Néel DWs described previously persists in the presence of disorder. This is shown in Supplementary Notes 6 and 7 as well as the Supplementary Movie 7. In particular, our systematic study reveals that J_c, the critical current at which kink nucleation is triggered, decreases with disorder (Fig. S.4a), which shows that disorder promotes kink nucleation.

Conclusions

In the present work, we demonstrated that achiral Néel DWs stabilized via in-plane strain and driven by SOT exhibit unique dynamics. We showed that these DWs stop moving above a certain threshold current density and that their internal magnetic moments exhibit spatial modulation characterized by a 180° rotation and ripple-like distortion of the DW shape. We revealed that, in contrast to DWs confined in narrow strips that stop moving due to torque cancellation, achiral DWs in wide strips stop due to the balance between the diffusive torque from exchange interaction, spin-orbit torque, and the anisotropy torque. We found that as long as this balance is maintained, the DW exhibits stationary behavior. However, if this balance is disrupted, the DW exhibits complex nonlinear behavior, where it either recovers its motion and oscillates continuously over time, or it breaks into multiple domains and recovers periodically. We linked our results to the dissipative solitons observed in other physical systems such as mode-locked lasers and reaction–diffusion systems. Our work reports the first theoretical prediction of DWs' solitonic pulsation and explosion, paving the way for exploring complex spatio-temporal dynamics in magnetic textures. These dynamics hold potential for applications in logic and neuromorphic computing.

Method

Micromagnetic simulations

Micromagnetic simulations are carried out using Mumax3[48] for a nanostrip of length $L = 1024$ nm, thickness $t_{FM} = 1$ nm, and variable width W using

1 nm cubic cells for spatial discretization. Since we are interested in studying DW dynamics on time scales up to microseconds and to avoid the effects of the DW interacting with the left and right edges, we shift the simulation frame to keep our DW always close to the center, fulfilling the condition $\langle m_z \rangle \approx 0$. The following magnetic and elastic material parameters are adopted in this work, corresponding to Co/Pt interfaces: $A_{ex} = 20$ pJ m^{-1} (exchange constant), $M_s = 0.58$ MA m^{-1} (saturation magnetization), $K_u = 0.9$ MJ m^{-3} (uniaxial anisotropy), $\alpha = 0.08$ (Gilbert damping), $\theta_{sh} = -0.33$ (spin Hall angle), $\lambda_s = -5 \times 10^{-5}$ (magnetostrictive coefficient), $C_{11} = 218$ GPa and $C_{12} = 133$ GPa (elastic constants). The SOT is given by $\boldsymbol{\tau}_{\rm SOT} = -\gamma \frac{\hbar \theta_{\rm SH} J}{2|e| M_s t_{\rm FM}} \boldsymbol{m} \times (\boldsymbol{m} \times \boldsymbol{\sigma})$, where γ is the gyromagnetic ratio, $\hbar$ is the reduced Planck constant, e is the electron charge, $\boldsymbol{\sigma} = \boldsymbol{u}_{\rm J} \times \boldsymbol{u}_z = -\boldsymbol{u}_y$ is the spin current polarization, and $\boldsymbol{u}_{\rm J}$ is the unit vector along the applied current direction. The corresponding SOT field can be expressed as $\boldsymbol{H}_{\rm SOT} = \frac{\hbar \theta_{\rm SH} J}{2|e| \mu_0 M_s t_{\rm FM}} \boldsymbol{\sigma}$. On the other hand, the magnetoelastic field is given by $\boldsymbol{H}_{\rm me} = \frac{2B_1}{\mu_0 M_s} \varepsilon_{\rm xx} m_x \boldsymbol{u}_x$, where $B_1 = \frac{3}{2} \lambda_s (C_{11} - C_{12}) = -6.375 \times 10^6$ J m^{-3} is the first magnetoelastic constant. A uniform longitudinal strain in the range of $\varepsilon_{\rm xx} = 0.005$–$0.03$ is used throughout this work.

Data availability

The data supporting the findings of this study are available from the corresponding authors upon reasonable request.

Code availability

The codes used to analyze the data and to solve the model partial differential equations are available from the corresponding authors upon reasonable request.

Received: 30 October 2024; Accepted: 21 May 2025;
Published online: 04 June 2025

References

1. Cross, M. C. & Hohenberg, P. C. Pattern formation outside of equilibrium. *Rev. Mod. Phys.* **65**, 851 (1993).
2. Cross, M. & Greenside, H. *Pattern Formation and Dynamics in Nonequilibrium Systems* (Cambridge Univ. Press, 2009).
3. Ankiewicz, A. & Akhmediev, N. *Dissipative Solitons: From Optics to Biology and Medicine* (Springer, 2008).
4. Turing, A. The chemical basis of morphogenesis. *Philos. Trans. R. Soc. Lond. B* **237**, 37–72 (1952).
5. Kicheva, A., Cohen, M. & Briscoe, J. Developmental pattern formation: insights from physics and biology. *Science* **338**, 210–212 (2012).
6. Koch, A.-J. & Meinhardt, H. Biological pattern formation: from basic mechanisms to complex structures. *Rev. Mod. Phys.* **66**, 1481 (1994).
7. Rüdiger, S. & Feudel, F. Pattern formation in Rayleigh-Bénard convection in a cylindrical container. *Phys. Rev. E* **62**, 4927 (2000).
8. Thomas, D., Sureshkumar, R. & Khomami, B. Pattern formation in Taylor-Couette flow of dilute polymer solutions: dynamical simulations and mechanism. *Phys. Rev. Lett.* **97**, 054501 (2006).
9. Arecchi, F. T., Boccaletti, S. & Ramazza, P. Pattern formation and competition in nonlinear optics. *Phys. Rep.* **318**, 1–83 (1999).
10. van Dijken, S. *Pattern Formation and Magnetic Anisotropy in Thin Metal Films*. Ph.D. thesis (FU Berlin, 2000).
11. Akhmediev, N. & Ankiewicz, A. *Dissipative Solitons in the Complex Ginzburg-Landau and Swift-Hohenberg Equations* 1–17 (Springer, Berlin, 2005).
12. Christov, C. & Velarde, M. Dissipative solitons. *Phys. D Nonlinear Phenom.* **86**, 323–347 (1995).
13. Purwins, H.-G., Bödeker, H. & Amiranashvili, S. Dissipative solitons. *Adv. Phys.* **59**, 485–701 (2010).
14. Friedlander, S. & Lipton-Lifschitz, A. Chapter 8 - localized instabilities in fluids. In *Handbook of Mathematical Fluid Dynamics*, Vol. 2 289–354 (North-Holland, 2003).
15. Dudley, J. M., Dias, F., Erkintalo, M. & Genty, G. Instabilities, breathers and rogue waves in optics. *Nat. Photonics* **8**, 755–764 (2014).
16. Mohseni, S. M. et al. Spin torque–generated magnetic droplet solitons. *Science* **339**, 1295–1298 (2013).
17. Grollier, J. et al. Neuromorphic spintronics. *Nat. Electron.* **3**, 360–370 (2020).
18. Kosiński, R. A. Spatio-temporal diagrams for domain wall dynamics. *Phys. Lett. A* **169**, 263–268 (1992).
19. Kosinski, R. Range of chaotic motion of a domain wall in a periodic drive field. *J. Appl. Phys.* **73**, 320–322 (1993).
20. Schryer, N. L. & Walker, L. R. The motion of 180° domain walls in uniform DC magnetic fields. *J. Appl. Phys.* **45**, 5406–5421 (1974).
21. Alejos, O., Raposo, V. & Martinez, E. *Domain Wall Motion in Magnetic Nanostrips*, ch. 5, 1–49 (John Wiley and Sons, Ltd, 2020).
22. Kim, J., Akinaga, H. & Kim, J. Direct observation of the spin configurations of vertical Bloch line. *Appl. Phys. Lett.* **98**, 052510 (2011).
23. Herranen, T. & Laurson, L. Domain walls within domain walls in wide ferromagnetic strips. *Phys. Rev. B* **92**, 100405 (2015).
24. Herranen, T. & Laurson, L. Bloch-line dynamics within moving domain walls in 3d ferromagnets. *Phys. Rev. B* **96**, 144422 (2017).
25. Yoshimura, Y. et al. Soliton-like magnetic domain wall motion induced by the interfacial Dzyaloshinskii–Moriya interaction. *Nat. Phys.* **12**, 157–161 (2016).
26. Purwins, H.-G., Bödeker, H. & Liehr, A. *Dissipative Solitons in Reaction-Diffusion Systems* 267–308 (Springer, Berlin, 2005).
27. Franke, K. J. A., Ophus, C., Schmid, A. K. & Marrows, C. H. Switching between magnetic Bloch and néel domain walls with anisotropy modulations. *Phys. Rev. Lett.* **127**, 127203 (2021).
28. Fattouhi, M. et al. Absence of walker breakdown in the dynamics of chiral Neel domain walls driven by in-plane strain gradients. *Phys. Rev. Appl.* **18**, 044023 (2022).
29. Haltz, E., Franke, K. J. & Marrows, C. H. Dynamics of bistable Néel domain walls under spin-orbit torque. *Phys. Rev. B* **109**, 064406 (2024).
30. Boulle, O. et al. Domain wall tilting in the presence of the Dzyaloshinskii-Moriya interaction in out-of-plane magnetized magnetic nanotracks. *Phys. Rev. Lett.* **111**, 217203 (2013).
31. Slonczewski, J. Dynamics of magnetic domain walls. *AIP Conf. Proc* **5**, 170–174 (1972).
32. Zhang, X. et al. Direct observation of domain-wall surface tension by deflating or inflating a magnetic bubble. *Phys. Rev. Appl.* **9**, 024032 (2018).
33. Morris, R. The dilogarithm function of a real argument. *Math. Comput.* **33**, 778–787 (1979).
34. Guslienko, K. Y. & Slavin, A. N. Boundary conditions for magnetization in magnetic nanoelements. *Phys. Rev. B* **72**, 014463 (2005).
35. Skaugen, A. & Laurson, L. Depinning exponents of thin film domain walls depend on disorder strength. *Phys. Rev. Lett.* **128**, 097202 (2022).
36. Madzvamuse, A., Ndakwo, H. S. & Barreira, R. Cross-diffusion-driven instability for reaction-diffusion systems: analysis and simulations. *J. Math. Biol.* **70**, 709–743 (2015).
37. Guin, L. N., Djilali, S. & Chakravarty, S. Cross-diffusion-driven instability in an interacting species model with prey refuge. *Chaos Solitons Fractals* **153**, 111501 (2021).
38. Wang, F. & Yang, R. Spatial pattern formation driven by the cross-diffusion in a predator-prey model with holling type functional response. *Chaos Solitons Fractals* **174**, 113890 (2023).
39. Braun, H.-B. Topological effects in nanomagnetism: from superparamagnetism to chiral quantum solitons. *Adv. Phys.* **61**, 1–116 (2012).
40. Soto-Crespo, J. M., Akhmediev, N. & Ankiewicz, A. Pulsating, creeping, and erupting solitons in dissipative systems. *Phys. Rev. Lett.* **85**, 2937–2940 (2000).

41. Soto-Crespo, J. M. & Akhmediev, N. Soliton as strange attractor: nonlinear synchronization and chaos. *Phys. Rev. Lett.* **95**, 024101 (2005).
42. Grelu, P. & Akhmediev, N. Dissipative solitons for mode-locked lasers. *Nat. Photonics* **6**, 84–92 (2012).
43. Descalzi, O., Akhmediev, N. & Brand, H. R. Exploding dissipative solitons in reaction-diffusion systems. *Phys. Rev. E* **88**, 042911 (2013).
44. Kataja, M. & van Dijken, S. Magneto-optical Kerr effect susceptometer for the analysis of magnetic domain wall dynamics. *Rev. Sci. Instrum.* **82**, 103901 (2011).
45. Boehm, B. et al. Achiral tilted domain walls in perpendicularly magnetized nanowires. *Phys. Rev. B* **95**, 180406 (2017).
46. Avci, C. O., Beach, G. S. D. & Gambardella, P. Effects of transition metal spacers on spin-orbit torques, spin hall magnetoresistance, and magnetic anisotropy of Pt/Co bilayers. *Phys. Rev. B* **100**, 235454 (2019).
47. Nan, T. et al. Comparison of spin-orbit torques and spin pumping across NiFe/Pt and NiFe/Cu/Pt interfaces. *Phys. Rev. B* **91**, 214416 (2015).
48. Vansteenkiste, A. et al. The design and verification of MuMax3. *AIP Adv.* **4**, 107133 (2014).

Acknowledgements

We gratefully acknowledge financial support from the European Union H2020 Program under (MSCA MagnEFi ITN Grant Number 860060), from Ministerio de Ciencia, Innovacion y Universidades under (PID2023-150853NB-C31 and PID2022-136285NB-C32), and from Department of Education of Junta de Castilla y Leon and FEDER Funds under (SA106P23 and CLU-2023-1-02).

Author contributions

M.F. and L.L.D. conceived the idea. E.M. and L.L.D. supervised the work. A.T. contributed and supervised the theoretical part. M.F. performed micromagnetic simulation and analytical calculation. F.G.S. assisted with micromagnetic simulations and data analysis. R.O. and M.P.G.E. assisted with the analytical calculations. M.F. carried out the data analysis. All authors contributed to the analysis and interpretation of the results. M.F. and L.L.D. wrote the original manuscript draft. All authors contributed to the revised manuscript version.

Competing interests

The authors declare no competing interests.

Additional information

Supplementary information The online version contains supplementary material available at https://doi.org/10.1038/s42005-025-02155-5.

Correspondence and requests for materials should be addressed to Mouad Fattouhi.

Peer review information *Communications Physics* thanks Sougata Mallick and the other anonymous reviewer(s) for their contribution to the peer review of this work.